Journal of Physics:
Conference Series

PAPER • **OPEN ACCESS**

Design and hydrodynamic coefficient identification of deep-sea unmanned underwater vehicles

To cite this article: Houyuan Hua *et al* 2025 *J. Phys.: Conf. Ser.* **3098** 012028

Journal of Physics: Conference Series **3098** (2025) 012028 doi:10.1088/1742-6596/3098/1/012028

Design and hydrodynamic coefficient identification of deep-sea unmanned underwater vehicles

Houyuan Hua, Zhen Zhang, Huarui Wang, Wenjing Yu*

Institute of Noise and Vibration, Naval University of Engineering, National Key Laboratory on Ship Vibration and Noise, Naval University of Engineering, Wuhan, 430033, China

*Corresponding author's e-mail: 1820184334@nue.edu.cn

Abstract. This study initially designed a deep-sea unmanned underwater vehicle (UUV) employing a double-hull pressure-resistant structure, resolving pressure containment challenges through a three-tier protective system comprising "pressure-bearing inner hull, oil-filled buffer layer, and flow-guiding outer shell." Subsequently, computational fluid dynamics (CFD) methodology was employed to conduct flow field analysis and numerical simulations of the vehicle. Ultimately, the acquisition of key hydrodynamic coefficients for the UUV was achieved through multiple linear regression methodology. This research establishes theoretical foundations for deep-sea UUV design, with particular emphasis on the derivation of critical hydrodynamic coefficients, providing essential support for subsequent motion control modeling of autonomous underwater vehicles (AUVs).

1. Introduction

In recent years, scholars both domestically and internationally have conducted extensive research on oil-filled seal-related structures. Feng Sen [1] proposed an oil-filled self-compensating module structure, which utilizes the pressure difference between the inner and outer chambers to drive hydraulic oil for automatic compensation, significantly enhancing the operational reliability of small underwater robot propulsion systems; Cao Gang et al. [2], Based on the principle of rolling diaphragm pressure compensators, a new type of pressure compensator enabling ROVs to operate at depths of 5,000 meters without the need for heavy-duty pressure-resistant structures; Hu Kai et al. [3], by studying the influence of water pressure on the compressibility of hydraulic oil, established a mathematical model of the volume elastic modulus of transformer oil as a function of water depth; Ma Yunxiang [4] designed an energy-saving hydraulic buoyancy control device that can optimize the buoyancy state and navigation attitude of autonomous underwater vehicles, effectively reducing control difficulty and navigation resistance; Fengrui Zhang et al. [5] designed a hydraulic-oil bladder deep-sea buoyancy control system consisting of pressure-resistant glass half-shells, titanium rings, and oil bladders, with a maximum design diving depth of 6,000 meters.

Currently, scholars at home and abroad are continuously improving the theoretical foundations of underwater vehicle dynamics, employing numerical methods to study their motion characteristics. Research methods have evolved from mathematical analytical methods, Eulerian methods, and surface element methods to computational fluid dynamics (CFD) methods utilizing computer technology. The objects of study have also progressed from simple to complex, expanding from initial rotating bodies (such as spheres and cylinders) to objects of general shapes. Analytical methods, as the initial paradigm in fluid mechanics research, use mathematical tools to construct physical models. However, they are limited by computational complexity and geometric simplification. Hicks [6] first employed the continuous mapping method to solve the flow field interference problem between two spherical bodies, proposing a dipole superposition solution, which opened new avenues for analytical solutions under complex boundary conditions. Basset [7], based on the continuous potential theory, revealed the correlation between flow field velocity potential and object geometric parameters, and derived additional mass coefficients. Lamb [8] constructed a kinetic energy-momentum conversion model for multi-body systems using the Lagrange equation, enabling the prediction of internal force distributions in flow fields. However, analytical methods are only applicable to ideal fluids and simple geometries, limiting their engineering applications. The Euler method is based on Newton's laws of motion and improves computational accuracy through grid discretization. Joe. F [9] proposed a boundary-fitting coordinate system technique that enables automatic grid generation for complex geometries, significantly improving the agreement between numerical solutions and experimental data. K.P. Singh et al. [10,11] combined the Runge-Kutta integration scheme with unstructured grids to successfully solve compressible Euler equations, expanding the analytical capabilities for moving boundary problems.

Fu Shuai [12] used the computational fluid dynamics software STAR-CCM+ to solve the RANS equations, employing spatially discrete structured grid technology to simulate hydrodynamics during single-ship navigation after validating the effectiveness of the numerical method. The surface element method (discrete boundary integral method) overcomes geometric limitations through a singularity distribution strategy. Hess and Smith [13] established a three-dimensional surface source-sink model based on Green's formula and proposed a numerical solution for velocity potential and pressure distribution. Joseph M. D'sa [14] compared axial and surface singularity distribution methods, pointing out the advantages of the latter in describing complex geometries. In domestic research, Chen Xiaoxing [15], based on potential flow theory, used COMSOL software and the boundary element method to perform numerical calculations of inertial-type hydrodynamic coefficients for a towed body; Zhang Ping [16], to improve the mathematical motion model of a submersible during strong maneuvering at high angles of attack, employed hexahedral unstructured grids to calculate the forces acting on the submersible at high angles of attack and obtained the hydrodynamic coefficients of the submersible through regression analysis. Since the 21st century, CFD technology, leveraging advancements in computer performance, has become the mainstream tool for fluid mechanics research. Its core advantages include: deepening of physical models: by solving the Navier-Stokes equations, it simultaneously considers fluid viscosity and complex boundary conditions, overcoming the limitations of the ideal fluid assumption[21]; expansion of engineering applications: covering automotive aerodynamic design [17], maneuverability prediction for underwater vehicles [18], medical vascular diseases [19], and other fields; algorithm innovation: the SST-DES turbulence model [20], overlapping-sliding hybrid mesh technology [18], significantly enhancing the simulation accuracy of flow separation and unsteady effects[23].

This paper establishes and optimizes a three-dimensional model of an underwater unmanned vehicle and selects appropriate CFD software for flow field analysis. By comparing and selecting the best hydrodynamic performance curves for the bow and stern, this paper analyzes the key hydrodynamic acquisition methods for existing underwater unmanned vehicles and selects an appropriate and economical hydrodynamic acquisition method to achieve the key hydrodynamic acquisition for underwater unmanned vehicles. The full text is organized as follows:

1. Main structure and parameters. The UUV is designed with a double-hull pressure-resistant structure, employing a three-layer protective system of "inner hull pressure resistance-oil bladder cushioning-outer hull flow diversion," and key technical parameters are provided.

2. Hydrodynamic acquisition theoretical foundation. The basic principles of CFD are introduced, and the computational fluid dynamics simulation software Star-CCM+ is selected for computational domain and boundary condition setup, followed by mesh partitioning and numerical method validation, with final analysis of simulation results.

3. Identification of hydrodynamic coefficients using a multiple linear regression method. Parameters such as force and torque were obtained under different operating conditions in both vertical and horizontal planes. The data were fitted to obtain equations, and the coefficients were dimensionless by normalizing the slope or intercept to derive the hydrodynamic coefficients.

2. Research Foundation

2.1 Theoretical Foundation

In hydrodynamic modeling, four principal methodologies dominate hydrodynamic coefficient acquisition: 1) Experimental measurement of physical prototypes; 2) Semi-theoretical/semi-empirical estimation methods; 3) System identification using operational data[22]; 4) CFD-based simulation methods[26]. Comparative analysis reveals CFD's distinct advantages over alternative approaches: lower capital expenditure, capacity to simulate complete operational profiles under various working conditions, extended experimental scope beyond physical testing limitations, reduced experimental expenditures and workload, and enhanced configuration flexibility. These attributes position CFD as the most cost-efficient and operationally versatile solution for comprehensive hydrodynamic characterization of underwater vehicles.

The application of CFD methodology inherently adheres to three fundamental conservation principles governing fluid motion: the law of energy conservation, mass conservation, and momentum conservation. The mathematical formulations derived from these universal physical laws constitute the Navier-Stokes equations.

Momentum Conservation Equation:

$$\frac{\partial(\rho u_i)}{\partial t}+div(\rho u_i u)=-\frac{\partial p}{\partial x_i}+\frac{\partial \tau_{xx_i}}{\partial x}+\frac{\partial \tau_{yx_i}}{\partial y}+\frac{\partial \tau_{zx_i}}{\partial z}+F_{xi} \tag{1}$$

In the momentum conservation equations, τ_{xx_i}, τ_{yx_i}, τ_{zx_i} represent the components of viscous force τ acting on the surface of the differential fluid element; u denotes the velocity vector, while u_i signifies the projection of the velocity vector in an arbitrary direction; ρ corresponds to the fluid density; p represents the pressure acting on the differential element; F_{x_i} indicates the components of the volume force on the differential element in each direction. When the volume force solely comprises gravity acting vertically upward, $F_z=-\rho g$ and $F_x=F_y=0$.

Continuity equation:

$$\frac{\partial \rho}{\partial t}+\frac{\partial(\rho u)}{\partial x}+\frac{\partial(\rho v)}{\partial y}+\frac{\partial(\rho \omega)}{\partial z}=0 \tag{2}$$

When dealing with incompressible fluids where the fluid density remains constant, Equation (2) can be simplified to:

$$\frac{\partial u}{\partial x}+\frac{\partial v}{\partial y}+\frac{\partial \omega}{\partial z}=0 \tag{3}$$

Energy conservation equation:

In this research, the underwater vehicle operates in marine environments characterized by viscous incompressible flow at low Reynolds numbers, where thermal effects on water's physical properties are essentially disregarded in motion calculations. Consequently, only mass conservation and momentum conservation principles govern the hydrodynamic analysis.

2.2 Turbulence Model

Common turbulence models primarily include: SST k-ω model, standard k-ε model, RNG k-ε model, and baseline k-ω model. In this study, the SST k-ω model is employed in numerical simulations due to its superior capability in capturing fluid motion characteristics, and will consequently be adopted for subsequent software simulations[25]. Particular analytical focus is directed toward the SST k-ω model, whose distinguishing feature lies in its enhanced performance for Reynolds-averaged Navier-Stokes (RANS) solutions within wall-bounded flows, particularly effective for boundary layer dynamics under adverse pressure gradients and flow separation scenarios.

The transport equation for turbulent kinetic energy (k) is expressed as:

$$\frac{\partial}{\partial t}(\rho \mathrm{k})+\frac{\partial}{\partial x_i}(\rho \mathrm{k} u_i)=\frac{\partial}{\partial x_i}\left[\Gamma_k \frac{\partial k}{\partial x_j}\right]+\tilde{\mathrm{G}}_{\mathrm{k}}-Y_k+S_k \tag{4}$$

The transport equation governing the turbulent dissipation rate (ω) is formulated as:

$$\frac{\partial}{\partial t}(\rho\omega)+\frac{\partial}{\partial x_i}\left(\rho\omega u_i\right)=\frac{\partial}{\partial x_j}\left[\Gamma_\omega\frac{\partial\omega}{\partial x_j}\right]+\tilde{G}_\omega-Y_\omega+D_\omega+S_\omega \tag{5}$$

In the equations, Γ_k and Γ_ω represent the effective diffusion of *k* and *ω,* respectively; $\tilde{G}_k$ is the production term of turbulent kinetic energy *k*; $\tilde{G}_\omega$ is the production term of turbulent dissipation rate *ω*; Y_k and Y_ω denote the turbulent dissipation terms of *k* and *ω,* respectively; S_k and S_ω indicate user-defined source terms; D_ω represents the cross-diffusion term.

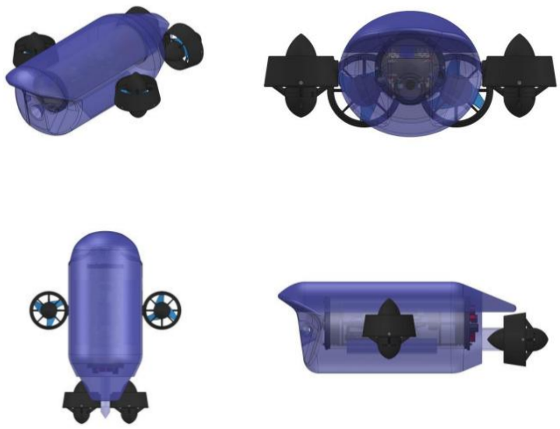

Figure 1. Three-dimensional configuration schematic of the model.

2.3 Model Foundation

The paramount technical challenge in deep-sea unmanned underwater vehicles lies in pressure resistance resolution. This study adopts a double-shell architecture comprising a pressure-resistant inner hull and a non-pressure-resistant outer shell. The vehicle features a spindle-shaped hydrodynamic profile (total length 0.55 m, maximum width 0.47 m) with tri-layer construction: Core layer-internal pressure hull (housing control systems and power modules); buffer layer-oil-filled compartment between hulls (average thickness 4 cm); flow-guiding layer-external non-pressure shell (integrating propulsion system and detection equipment). The three-dimensional structure diagram of the spacecraft and the table of key technical parameters are shown in Figure 1 and Table 1.

Table 1. Key Technical Parameters Table.

Name	Parameter
Overall Length	60cm
Overall Width	47.15cm
Overall Height	20.4cm
Mass	4.0647kg
Volume	3.05×10^{-3}m^3
Surface Area	1.904m^2
Center of Gravity	X = 0.01mm Y = 39.63mm Z = 117.64mm
Moment of Inertia	Ix = (0, -0.05, 1) Px = 46604157.95 Iy = (1, 0, 0) Py = 92456898.07 Iz = (0, 1, 0.05) Pz = 128029278.77

3. Condition Settings

3.1 Computational Domain and Boundary Conditions

A rectangular fluid computational domain measuring 7 L × 4 L × 4 L (length × width × height) is established. For bow-on inflow conditions, the left boundary is specified as a velocity inlet boundary condition, the right boundary as a pressure outlet boundary condition, and the remaining boundaries as symmetry planes. The velocity inlet is positioned 2 L upstream from the vehicle's bow, while the pressure outlet is located 5 L downstream from the stern. The vehicle is centered within the domain's right-view plane, with seawater as the working fluid. Local grid refinement is implemented at critical regions, including bow protrusions, propeller thrusters, and wake zones, as detailed in the grid schematic. Constant-density segregated flow model is activated with partial parameters, retaining default values. The computational domain configuration is illustrated in Figure 2.

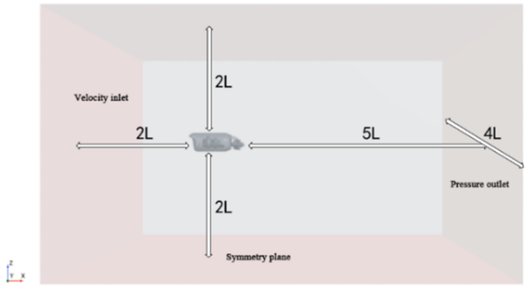

Figure 2. Computational domain configuration schematic.

3.2 Grid Generation

Polyhedral mesh methodology is employed for grid generation, with post-discretization mesh cross-sectional views illustrated in Figure 3.

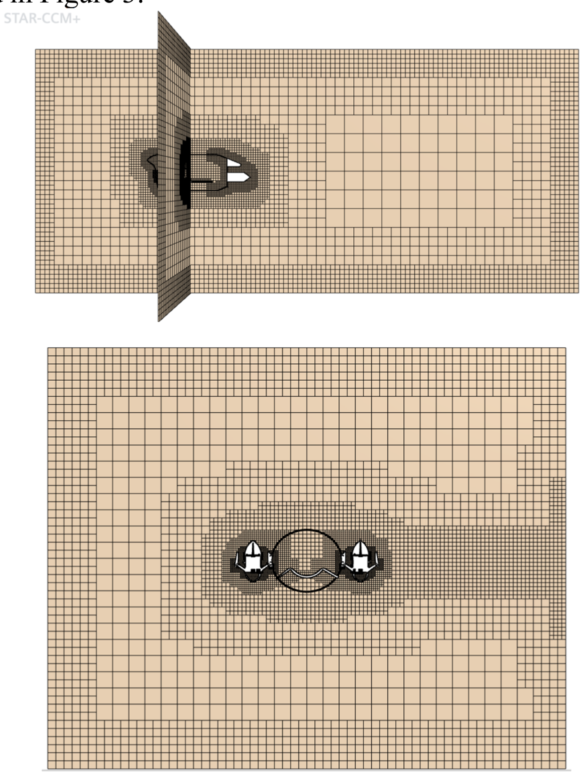

Figure 3. Volume Mesh Generation.

3.3 Numerical Method Verification

To verify the consistency and reliability of simulation results under different grid sizes, this study conducts grid independence verification for the computational model. By progressively reducing the base grid size while maintaining grid topology and quality, the variation trends of numerical solutions are analyzed. A threshold of $\leq 10\%$ change rate between adjacent grid resolutions is established as validation criteria.

As the designed vehicle lacks reference numerical data for direct validation, the SUBOFF model is selected for comparative verification. Following ITTC recommended procedures, the base grid size is scaled from 0.2 m to 0.05 m (two downward refinements and two upward coarsenings relative to the 0.1 m baseline), with corresponding mesh counts increasing from 1.66×10^5 to 2.38×10^6. The X-direction resistance values of the SUBOFF model during straight-ahead navigation at zero angle of attack under different mesh resolutions are compared, with convergence trends shown in Table 2.

Table 2. Grid Independence Verification Experimental Data Log Table.

Grid Size (m)	Mesh Count (elements)	Computed Value (N)
0.2	166610	63.98
0.14	275234	60.47
0.1	530827	59.49
0.077	1073166	59.10
0.05	2380319	58.87

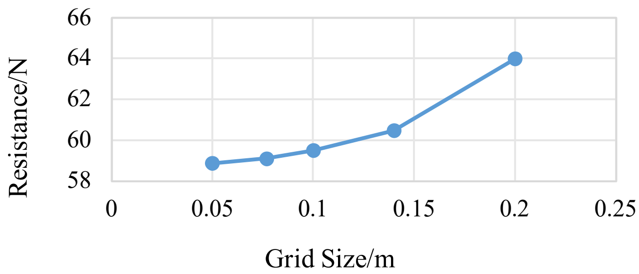

Figure 4. Schematic of Mesh Count and Computed Value Variations under Different Base Grid.

As shown in Table 2 and Figure 4, the X-direction resistance of the SUBOFF model converges toward a constant value with increasing mesh count, indicating that grid resolution effects on experimental results fall within an acceptable range. This confirms compliance with grid independence verification requirements for the numerical simulations. Through comparative analysis of experimental data, the optimal grid configuration is determined as a base grid size of 0.1 m and a total mesh count of 5.3×10^5, selected as fundamental parameters for subsequent computational model validation.

3.4 Result Validity Verification

The validation model employed in this section follows the configuration established in the preceding section, with internal iterations set to 10 and a maximum physical time of 5 s. Varying inflow velocity components simulate different angles of attack for the SUBOFF model. The comparative results of SUBOFF model angles of attack, computational outcomes from this study, and experimental measurements from referenced literature are tabulated in Table 3.

Table 3. Result Validity Verification Data Log Table.

Angle of Attack (°)	Simulated Value (N)	Simulated Value (N)	Error
0.00	118.98	132.14	9.96%
4.05	120.24	130.71	8.01%
11.96	106.20	110.62	4.00%
18.09	67.46	62.96	7.15%

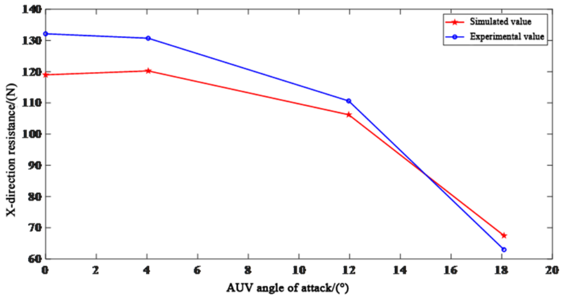

Figure 5. Computational Error Curve at Different Angles of Attack.

As shown in Table 3 and Figure 5, the prediction error of the adopted mesh configuration, parameters, and computational methodology compared to experimental values is less than 10 %, meeting the simulation accuracy requirements. This model can be used for subsequent simulations.

3.5 Analysis of Simulation Results

Following the initialization of simulation conditions, water flow impacts the vehicle within the test basin at prescribed velocity vectors while StarCCM+ monitors hydrodynamic resistance. During simulation, vertical plane velocity scalar plots visualize flow velocity magnitude/direction near the vehicle, complemented by horizontal plane pressure scalar plots depicting pressure distribution. The velocity and pressure scalar plots under stabilized 1 m/s flow conditions are presented below, as shown in Figure 6 and Figure 7.

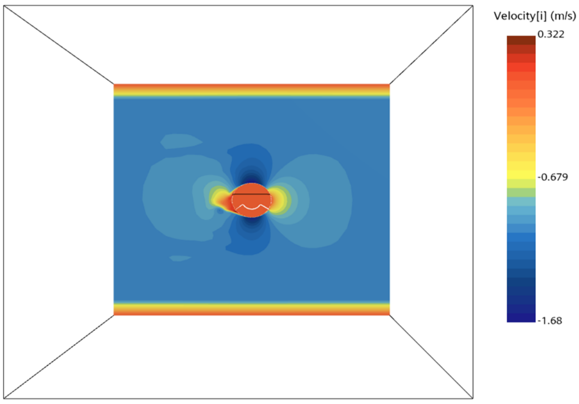

Figure 6. Velocity Scalar Plot.

Figure 7. Pressure Scalar Plot.

Observations from the velocity scalar plots reveal minimum flow velocity at the vehicle's bow and maximum velocity along the bow flank. Per Bernoulli's theorem ($p+\frac{1}{2}\rho v^2+\rho gh=C$), regions with maximum flow velocity exhibit minimal pressure, manifesting as light blue low-pressure zones

IOP Publishing
doi:10.1088/1742-6596/3098/1/012028

surrounding the bow. Conversely, reduced bow velocities generate red-hued high-pressure regions. Similar phenomena occur at the stern, though pressure distribution analysis via colorbar quantification demonstrates significantly higher bow pressures compared to the stern. This bow-stern pressure differential constitutes the primary source of hydrodynamic resistance acting on the vehicle[24].

4. Hydrodynamic Coefficient Identification Based on Multiple Linear Regression

4.1 Identification Condition Settings

The finalized model is imported into Star-CCM+ software for hydrodynamic coefficient acquisition experiments. In vertical plane simulations, inflow conditions are configured with longitudinal (X) and vertical (Z) velocity components (zero Y-direction velocity). The resultant velocity vector forms angles ranging from -8 ° to 8 ° relative to the X-axis, incremented in 2 ° steps. During each operational condition, triaxial forces (X/Y/Z) and moments about these axes are monitored, with data logging initiated upon reaching steady-state equilibrium. The coordinate vectors specified in the spacecraft are shown in Figure 8.

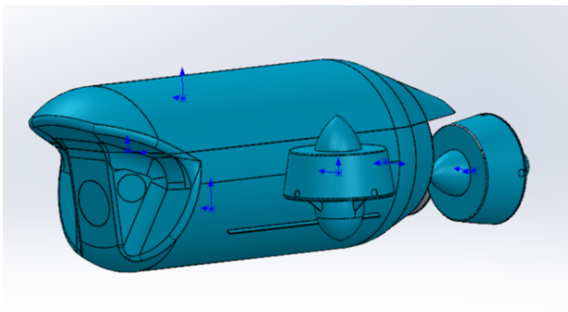

Figure 8. Underwater Vehicle Hydrodynamic Profile.

For horizontal plane simulations, inflow conditions combine longitudinal (X) and lateral (Y) velocity components (zero Z-direction velocity), while maintaining identical angular variation protocols and monitoring parameters as vertical plane configurations.

4.2 Parameter Identification

When navigating under ideal conditions, the underwater vehicle's motion determines the viscous hydrodynamic forces acting on its hull. For vertical and horizontal plane motions, attributing acceleration effects to acceleration coefficients, the viscous hydrodynamic forces can be expressed as:

$$\textit{Vertical plane motion}\begin{cases} X = f_x(u,v,r,\delta) \\ Y = f_y(u,v,r,\delta) \\ N = f_N(u,v,r,\delta) \end{cases} \tag{6}$$

$$\textit{Horizontal plane motion}\begin{cases} X = f_x(u,v,r,\delta) \\ Y = f_y(u,v,r,\delta) \\ N = f_N(u,v,r,\delta) \end{cases} \tag{7}$$

(1) Zero-Lift Force Coefficient $Z_0^{'}$ and Zero-Lift Moment Coefficient $M_0^{'}$

When the underwater vehicle undergoes steady rectilinear motion at a specific velocity u_0, its lateral velocity, angular velocities, horizontal fin angles, and all accelerations are zero. Due to the vertical asymmetry of the vehicle, a zero-lift force Z_0 exists, and its longitudinal asymmetry results in a zero-lift moment M_0. Non-dimensionalization of these two quantities yields:

$$\begin{cases} Z_0 = Z_0' \times \left(\frac{1}{2} \rho v^2 L^2 \right) \\ M_0 = M_0' \times \left(\frac{1}{2} \rho v^2 L^3 \right) \end{cases} \tag{8}$$

(2) Horizontal fin angle coefficient Z_δ' and M_δ'

When the horizontal fins are deflected at specific angles during the vehicle's steady rectilinear motion at velocity u_0, vertical forces and pitching moments are simultaneously generated. These parameters can be non-dimensionalized as:

$$\begin{cases} Z(\delta) = Z_\delta' \times \left(\frac{1}{2} \rho v^2 L^2 \delta^2 \right) \\ M(\delta) = M_0' \times \left(\frac{1}{2} \rho v^2 L^3 \delta \right) \end{cases} \tag{9}$$

(3) Vertical force coefficient Z_w' and Pitching moment coefficient M_w'

When the underwater vehicle moves under the combined action of longitudinal velocity and vertical velocity in water, it experiences vertical forces and pitching moments during the process. Since $W' = \frac{W}{V} = \sin\alpha$ and α is a small angle, $\sin\alpha$ can be equivalent to α, which represents the angle of attack of the vehicle's motion, indicating that such hydrodynamic forces are related to the vehicle's orientation relative to the flow direction. Non-dimensionalization can be expressed as:

$$\begin{cases} Z(w) = Z_w' \times \left(\frac{1}{2} \rho v L^2 w \right) \\ M(w) = M_w' \times \left(\frac{1}{2} \rho v L^3 w \right) \end{cases} \tag{10}$$

The underwater vehicle undergoes motion under combined longitudinal and lateral velocities, experiencing lateral force *Y(v),* yaw moment *N(v)* about the Z-axis, and roll moment *K(v)* about the X-axis during operation[22].

4.3 Application of stationary mesh numerical simulation

Numerical simulations of the vehicle's straight-ahead and oblique navigation processes are relatively straightforward. During experiments, the vehicle remains stationary relative to the test basin while simulating straight or oblique navigation conditions by adjusting the angle between the flow direction and coordinate axes, along with flow velocity.

For straight-ahead navigation along the X-direction, numerical simulations reveal that the vehicle experiences X-direction resistance, which increases with flow velocity. The relationship between flow velocity and X-direction resistance is detailed in Table 4 below.

Table 4. Result Validity Verification Data Log Table.

Navigation speed	**1**	**1.5**	**2**	**2.5**	**3**
X-direction force	-5.162	-10.8611	-18.54	-28.161	-39.636

The linear fitting method is reapplied to derive the governing equation, with subsequent non-dimensionalization of the slope yielding the X-direction resistance coefficient $X_u' = -1.66 \times 10^{-3}$ .The relationship between the obtained vertical force and the vertical flow velocity is presented in Table 5.

To determine the second-order vertical force coefficient $Z_{w|w|}$ and refine the zero-lift force Z_0' and zero-lift moment M_0', stationary mesh simulations are conducted with the test basin and vehicle maintaining relative stillness. Flow is configured along the Z-axis from negative to positive directions, initiating at 0.3 m/s and incrementing by 0.1 m/s per simulation cycle until reaching 1 m/s.

The total Z-direction force acting on the underwater vehicle can be expressed as:

$$Z = Z_0 + Z_w w + Z_{w|w|} w \,|\, w \,| \tag{11}$$

By reapplying the fitting method, the functional expression is derived. Based on Equation (11), the trendline polynomial is adjusted to second-order, yielding a quadratic equation where the quadratic term coefficient represents the second-order vertical force coefficient , and the constant term corresponds to the zero-lift force. This simulation can also be regarded as the vehicle's straight-line motion along the Z-direction, enabling simultaneous monitoring of longitudinal resistance and pitching moments. Final calculations yield: $Z_{w|w|}$ = -0.064, Z_0' = 0.0071, X_{ww}' = -0.0548, M_{ww}' = 0.0043. The zero-lift moment M_0' is similarly obtained, resulting in 0.00067.

Table 5. Result Validity Verification Data Log Table.

Flow velocity	Z-direction resistance
0.3	-16.63
0.4	-29.53
0.5	-43.3
0.6	-67.03
0.7	-88.63
0.8	-111.73
0.9	-139.12
1	-169.76

For oblique navigation in the horizontal plane, the vehicle remains stationary in the test basin while the inflow direction deviates incrementally from the negative X-axis by adjusting the drift angle from -8 ° to + 8 ° in 2 ° increments at 2 m/s. Numerical simulations capture lateral forces (Y), roll moments (K) about the X-axis, and yaw moments (N) about the Z-axis. Results are summarized in Table 6.

Table 6. Result Validity Verification Data Log Table.

Angle dependent force	0	2	4	6	8
X-direction force	18.1068	18.1213	18.1413	18.1916	18.2837
Y-direction force	-0.1658	0.663247	1.02885	1.2787	1.7
X-direction moment	0.0532	0.0194	-0.0038	-0.0602	-0.088
Z-direction moment	0.1879	1.855	3.6403	5.28364	7.1197

Data analysis reveals that increasing drift angles have a negligible impact on the magnitude of moments about the X-axis, with values remaining consistently minimal. Therefore, parameter K_0' is approximated as zero. Linear fitting of the results is performed, followed by non-dimensionalization of the slope to derive hydrodynamic coefficients $Y_v' = 2.53 \times 10^{-3}$ and $N_V' = 0.0104$. Similarly, non-dimensionalization of the intercept yields coefficients $Y_0' = 2.86 \times 10^{-4}$ and $N_0' = 1.584 \times 10^{-3}$.

4.4 Application of Dynamic Mesh Numerical Simulation

By conducting heavy motion simulations of the underwater vehicle in the test basin, parameters Z_w', M_w', and acceleration coefficients Z_w', M_w' can be calculated. The Dynamic Fluid-Body Interaction (DFBI) module is integrated into previous simulations to better simulate vehicle motion through fluid-structure coupling. The mesh is modified to a dynamic type, enabling synchronized motion between the test basin and the vehicle. DFBI parameters are configured as follows: body mass = 110.0 kg, motion type = planar motion vehicle (rigid-body planar motion category), with constraints set to "free heave" and "unconstrained roll" to maintain zero trim in the vertical plane while executing sinusoidal rigid-body motion. The vehicle's velocity along the X-axis is set to 0.5 m/s, with Z-axis oscillation amplitude of 0.04 m and a frequency of 0.8 Hz. The motion schematic is shown in Figure 9.

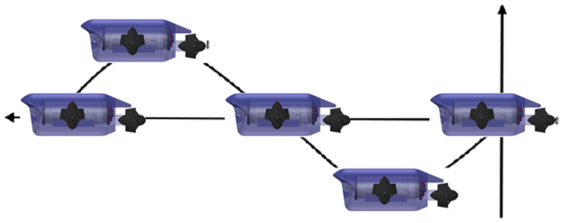

Figure 9. Heave Motion Schematic Diagram.

The vertical force acting on the vehicle is denoted as Z, and the pitching moment as M. Based on the equations of motion, the hydrodynamic force expressions can be derived as:

$$\begin{cases} Z = Z_{\dot{w}}\dot{w} + Z_w w + Z_0 = -a\omega^2 Z_{\dot{w}} \sin\omega t + a\omega Z_w \cos\omega t + Z_0 \\ M = M_{\dot{w}}\dot{w} + M_w w + M_0 = -a\omega^2 M_{\dot{w}} \sin\omega t + a\omega M_w \cos\omega t + M_0 \end{cases} \tag{12}$$

The aforementioned hydrodynamic parameters can be non-dimensionalized to obtain:

$$\begin{cases} Z'_w = \dfrac{Z_w}{\frac{1}{2}\rho L^2 V} \\ Z'_{\dot{w}} = \dfrac{Z_{\dot{w}}}{\frac{1}{2}\rho L^3} \\ M'_w = \dfrac{M_w}{\frac{1}{2}\rho L^3 V} \\ M'_{\dot{w}} = \dfrac{M_{\dot{w}}}{\frac{1}{2}\rho L^4} \end{cases} \tag{13}$$

Substituting Equation (12) into Equation (11) yields:

$$\begin{cases} Z = -\dfrac{1}{2}\rho L^3 a\omega^2 Z'_{\dot{w}} \sin\omega t + \dfrac{1}{2}\rho L^2 V a\omega Z'_w \cos\omega t + Z_0 \\ M = -\dfrac{1}{2}\rho L^4 a\omega^2 M'_{\dot{w}} \sin\omega t + \dfrac{1}{2}\rho L^3 V a\omega M'_w \cos\omega t + M_0 \end{cases} \tag{14}$$

By substituting hydrodynamic forces and moments into the variables of Equations (14) and (15) can be derived:

$$\begin{cases} Z_1 = -\dfrac{1}{2}\rho L^3 a\omega^2 Z'_{\dot{w}}, Z_2 = \dfrac{1}{2}\rho L^2 V a\omega Z'_w \\ M_1 = -\dfrac{1}{2}\rho L^4 a\omega^2 M'_{\dot{w}}, M_2 = \dfrac{1}{2}\rho L^3 V a\omega M'_w \end{cases} \tag{15}$$

The parameters Z_1, Z_2, M_1, and M_2 represent the hydrodynamic forces and moments acting on the vehicle during actual motion. Numerical simulations are employed to generate time-dependent curves for the Z-direction force and moments about the Y-axis. By selecting a stable oscillation cycle, curve fitting is performed to derive the expression $f(t)$. Assuming a total cycle length of $2l$, Fourier expansion is applied to $f(t)$ over the interval (−1,1), ultimately yielding a formula analogous to Equation (16).

$$f(t) = a_0 + a_1 \cos\frac{\pi t}{l} + b_1 \sin\frac{\pi t}{l} \tag{16}$$

By combining Equation (16) with the heave motion force and moment equations (Equation 12), values $a_{z1}, b_{z1}, a_{M1}, b_{M1}$ are obtained through curve fitting, corresponding to parameters Z_1, Z_2, M_1, M_2 in the preceding context. By calculating these data, the hydrodynamic coefficients $Z'_{\dot{w}}$ and $M'_{\dot{w}}$ can be solved. The computational results are presented in Table 7, with all hydrodynamic coefficients summarized in Table 8.

By conducting pure pitching motion of the underwater vehicle in the test basin, the angular velocity coefficients $Z_q^{'}$, $M_q^{'}$ and angular acceleration coefficients $Z_q^{'}$, $M_q^{'}$ can be obtained. In the "Planar Motion Vehicle" settings, select "General Planar Motion," "Free Heave," and "Free Pitch." Configure the X-direction velocity as 0.5 m/s, amplitude E = 0.04 m, frequency F = 10 Hz, and maintain zero heave velocity during motion.

Table 7. Computation results.

f(hz)	**0.8**
$\omega(1/s)$	**5.026**
$-\dfrac{aL\omega^2}{V^2}$	**-9.7**
$\dfrac{a\omega}{V}$	**0.402**
$\dfrac{Z_1}{0.5\rho L^2V^2}$	**0.073**
$\dfrac{Z_2}{0.5\rho L^2V^2}$	**-0.0072**
$\dfrac{M_1}{0.5\rho L^3V^2}$	**0.00121**
$\dfrac{M_2}{0.5\rho L^3V^2}$	**0.00197**

Table 8. Result Validity Verification Data Log Table.

Symbols of hydrodynamic coefficients	$Z_{\dot{w}}^{'}$	$Z_w^{'}$	$M_{\dot{w}}^{'}$	$M_w^{'}$
Value	-0.00752	-0.018	-0.00012	0.0049

During navigation, the vertical force acting on the vehicle is Z, and the pitching moment is M. The force expressions are:

$$\begin{cases} Z = -\theta_0\omega^2 Z_{\dot{q}} \sin\omega t + \theta_0\omega Z_q \cos\omega t + Z_0 \\ M = -\theta_0\omega^2 M_{\dot{q}} \sin\omega t + \theta_0\omega M_q \cos\omega t + M_0 \end{cases} \tag{17}$$

Non-dimensionalization of the aforementioned hydrodynamic parameters yields:

$$\begin{cases} Z_{\dot{q}} = \dfrac{\rho L^3}{2} Z_{\dot{q}}^{'} \\ Z_q = \dfrac{\rho L^2 V}{2} Z_q^{'} \\ M_{\dot{q}} = \dfrac{\rho L^4}{2} M_{\dot{q}}^{'} \\ M_q = \dfrac{\rho L^3 V}{2} M_q^{'} \end{cases} \tag{18}$$

Substituting Equation (18) into Equation (17) yields:

$$\begin{cases} Z = -\dfrac{\rho L^3\theta_0\omega^2}{2} Z_{\dot{q}}^{'} \sin\omega t + \dfrac{\rho L^2 V\theta_0\omega}{2} Z_q^{'} \cos\omega t + Z_0 \\ M = -\dfrac{\rho L^4\theta_0\omega^2}{2} M_{\dot{q}}^{'} \sin\omega t + \dfrac{\rho L^3 V\theta_0\omega}{2} M_q^{'} \cos\omega t + M_0 \end{cases} \tag{19}$$

By substituting hydrodynamic forces and moments into the variables of Equations (19) and (20) can be derived:

$$\begin{cases} Z_3 = -\dfrac{\rho L^3 \theta_0 \omega^2}{2} Z_{\dot{q}}', Z_4 = \dfrac{\rho L^2 V \theta_0 \omega}{2} Z_q' \\ M_3 = -\dfrac{\rho L^4 \theta_0 \omega^2}{2} M_{\dot{q}}', M_4 = \dfrac{\rho L^3 V \theta_0 \omega}{2} M_q' \end{cases} \tag{20}$$

The parameters Z_3, Z_4, M_3, and M_4 represent the hydrodynamic forces and moments acting on the vehicle during actual motion. By applying the data processing methodology used for heave motion analysis, the final results of pure pitching motion can be calculated, and the angular velocity and angular acceleration coefficients can be determined.The calculation results are shown in Table 9, and the hydrodynamic coefficients are presented in Table 10.

Table 9. Computation results.

$\omega(1/s)$	**10**
$-\dfrac{\theta_0 L \omega^2}{V^2}$	-38.4
$\dfrac{\theta_0 \omega}{V}$	0.802
$\dfrac{Z_3}{0.5\rho L^2 V^2}$	0.08817
$\dfrac{Z_4}{0.5\rho L^2 V^2}$	-0.0645
$\dfrac{M_3}{0.5\rho L^3 V^2}$	0.0721
$\dfrac{M_4}{0.5\rho L^3 V^2}$	-0.02396

Table 10. Result Validity Verification Data Log Table.

Hydrodynamic coefficients	**Underwater vehicle**
N_v'	-0.0104
Z_δ'	-0.0196
M_δ'	-0.00725
Z_0'	0.0071
M_0'	0.00067
$Z_{\dot{q}}'$	-0.0023
Z_q'	-0.084
$M_{\dot{q}}'$	-0.00187
M_q'	-0.0307
X_u'	-0.00166
K_0'	0

5. Conclusion

This study proposes a deep-sea autonomous underwater vehicle (AUV) design based on a double-hull pressure-resistant configuration, achieving structural integrity in extreme abyssal environments through a three-tier protection mechanism: “rigid inner hull pressure resistance - hydraulic oil compensation - streamlined outer hull flow guidance.” At the engineering implementation level, computational fluid dynamics (CFD) methods were employed to conduct multi-condition flow field simulations of the fully appended hull form. Numerical modeling utilizing Reynolds-averaged Navier-Stokes (RANS) equations with the SST k-ω turbulence model systematically evaluated hydrodynamic characteristics under varying speeds and angles of attack. For hydrodynamic parameter identification, a multivariate linear regression-based analytical approach was implemented to resolve critical hydrodynamic derivative coefficients. The developed parametric modeling methodology establishes a theoretical framework for deep-sea AUV hull design, with the acquired hydrodynamic coefficient dataset directly integrable into motion equations.

References

[1] Feng S. Design of a self-compensating underwater thruster and research on its sealing and hydrodynamic performance[J]. Lubrication and Sealing, 2022, 47(05): 141-147.
[2] Cao G, Wang H F, Zhang D H. Design research of a deep-sea ROV pressure compensator[J]. Control and Information Technology, 2024, (02): 105-110.
[3] Hu K, Xie Y W, Yu H L, et al. Optimization design of ROV compensation system[J]. Automation and Instrumentation, 2020, (06): 91-94.
[4] Ma Y X, Li L L, Chen Z D, et al. Energy-saving seawater hydraulic buoyancy adjustment system[J]. Hydraulics & Pneumatics, 2025, 49(1): 13-19.
[5] Zhang F R, Hou J, Ning D, et al. Depth control of an oil bladder type deep-sea AUV based on fuzzy adaptive linear active disturbance rejection control[J]. Machines, 2022, 10(3): 163.
[6] Hicks W M. On the motion of two spheres in a fluid[J]. Philosophical Transaction of the Royal Society London, 1880, 171(2): 455-492.
[7] Basset A B. On the motion of two spheres in a liquid, and allied problems[J]. Proceedings of the London Mathematical Society, 1887, 18: 369-378.
[8] Lamb H. Hydrodynamics (6th edition)[M]. Cambridge: Cambridge University Press, 1932.
[9] Thompson J F, Thames F C, Mastin C W. Automatic numerical generation of body-fitted curvilinear coordinate system for field containing any number of arbitrary two-dimensional bodies[J]. Journal of Computational Physics, 1974, 15: 299-319.
[10] Singh K P, Baysal O. Unstructured method for flows past bodies in general three-dimensional relative motion[J]. AIAA Journal, 2001, 39(2): 219-224.
[11] Singh K P, Newman J C, Baysal O. Dynamic unstructured method for flows past multiple objects in relative motion[J]. AIAA Journal, 1995, 33(4): 641-649.
[12] Fu S, Zhu Q Y, Shen LW. Numerical simulation of hydrodynamic interference between high-speed vessels nearby [J]. Shipbuilding of China, 2025, 66(1): 167-178.
[13] Hess J H, Smith A M. Calculation of nonlifting potential flow about arbitrary three-dimensional bodies[J]. Journal of Ship Research, 1964, 8(2): 22-44.
[14] D'Sa J M, Dalton C. Body of revolution comparisons for axial and surface-singularity distributions[J]. Journal of Aircraft, 1986, 23(8): 669-672.
[15] Chen X X, Hong Y C, Hu Y J. Rapid calculation method for inertial hydrodynamic coefficients of towed bodies[J]. Acoustics and Electronics Engineering, 2022(1): 16-18.
[16] Zhang P, Huang H F, Hu K, et al. Research on CFD-based calculation method for hydrodynamic coefficients of submerged bodies at high angles of attack[J]. Computer Simulation, 2023, 40(12): 41-45.
[17] Wang Q Y, Han M Y, Chang K Y, et al. CFD calculation of hydrodynamic parameters and maneuverability prediction for underwater vehicles[J]. China Offshore Platform, 2023, 38(01): 50-56.
[18] Zhou C K. CFD numerical analysis of navigation characteristics and influencing factors for underwater submersible systems[D]. South China University of Technology, 2021.
[19] Ding J, Ren B, Guo Y, et al. Advances in computational fluid dynamics applications for head and neck vascular lesions[J]. International Journal of Medical Radiology, 2025, 48(2): 223-228.
[20] You T Q, Wang Z Y, Cheng S H, et al. CFD calculation research on fluid damping force coefficients of underwater vehicles[J]. Missiles and Space Vehicles, 2016(1): 1004-7182.
[21] Chen T W, Wan D C. CFD analysis of motion resistance performance for underwater submersibles[J]. Journal of Hydrodynamics, 2018, 33(02): 143-149.
[22] Xiong H, Yan Z. A hydrodynamic coefficients reckon method and its application to robust heading control for underwater robot[C]//Proceedings of the 29th Chinese Control Conference. IEEE, 2010: 3219-3223.
[23] Zeng F. Numerical simulation and experimental study of hydrodynamic characteristics based on dynamic programming algorithm[C]//2022 IEEE 6th Advanced Information Technology, Electronic and Automation Control Conference (IAEAC). IEEE, 2022: 2033-2040.
[24] Bao H, Zhu H, Liu D. Research on hydrodynamic modeling and simulation of streamlined autonomous underwater vehicle based on CFD method[C]//2023 35th Chinese Control and Decision Conference (CCDC). IEEE, 2023: 4795-4800.
[25] Maciejewska B, Piasecka M, Dadas N, et al. Fluid flow and heat transfer characteristics in minichannels-CFD calculations in Simcenter STAR-CCM+[J]. Heat and Mass Transfer, 2025, 61(3): 22.
[26] Tu J, Yeoh G H, Liu C, et al. Computational Fluid Dynamics: A Practical Approach[M]. Elsevier, 2023.